JOURNAL OF SPACECRAFT AND ROCKETS
Vol. 47, No. 4, July–August 2010

Turbulent Supersonic/Hypersonic Heating Correlations for Open and Closed Cavities

Joel L. Everhart* and Francis A. Greene†
NASA Langley Research Center, Hampton, Virginia 23681

DOI: 10.2514/1.46877

An analysis of existing supersonic/hypersonic zero-pressure-gradient rectangular-geometry cavity heating data is presented, yielding new turbulent open-flow and closed-flow correlations for the floor-averaged heating and the peak endwall heating. Limited data recently acquired from the Space Shuttle Return-to-Flight Program were used to develop the closed-flow correlations. Historical data obtained from the literature, covering an extremely wide range of flow conditions and test facilities, were used to develop the open-cavity heating correlations. The correlations were developed using new parameters derived in terms of cavity geometry and local flow conditions. These parameters are linearly related with a linear correlation coefficient R^2, which exceeds 0.97 in all cases. Confidence-limit and prediction-limit uncertainty values are provided at the 99% level of significance.

Nomenclature

a, b	=	correlation curve-fit coefficients, see Eq. (2)
h	=	heat transfer coefficient, $q/(H_{aw} - H_w)$, lbm/ft^2/s
L, W, H	=	cavity length, width, and depth, in.
M	=	Mach number
M_e	=	boundary-layer edge Mach number at the cavity entrance
R^2	=	linear correlation coefficient
Re	=	unit Reynolds number, 1/ft
Re_θ	=	momentum-thickness Reynolds number
X, Y	=	correlation parameters, see Eq. (2).
x	=	axial distance from model leading edge, in.
y	=	spanwise distance from model centerline, in.
z	=	distance normal to x–y plane, in.
α	=	angle of attack, deg
α, β, σ, τ	=	bump-factor correlation coefficients, see Eq. (1)
δ	=	boundary-layer thickness, in.
θ	=	boundary-layer momentum thickness, in.

Subscripts

AVG	=	average value in cavity
Lam	=	laminar
MAX	=	maximum value on cavity centerline immediately downstream of endwall
Turb	=	turbulent
∞	=	freestream static conditions

I. Introduction

THE August 2003 Final Report of the Space Shuttle *Columbia* Accident Investigation Board [1] (CAIB) recommended the development of improved damage-assessment models for application to future flights, primarily for laminar flow conditions. In response, the Orbiter Entry Aeroheating Panel at the NASA Johnson Space Center established the Cavity Heating Team to develop the Cavity Heating Tool (CHT). This tool defines the heating augmentation to the vehicle outer mold lines caused by impact damage that does not penetrate the vehicle aluminum substructure. A survey of the cavity heating literature conducted for CHT development revealed that much general information was available on cavity flow physics and heating; however, information required to address Orbiter-specific damage was very sparse. For example, there was no information regarding the real-cavity effects of random geometry, crossflow, or pressure gradient. This sparseness led to an extensive series of supersonic/hypersonic idealized-cavity-flow experiments by Everhart et al. [2–6] that were conducted in the conventional 20-Inch Mach 6 and 31-Inch Mach 10 Wind Tunnels at the NASA Langley Research Center (LaRC). The idealized cavity geometries were rectangular boxes that were easily defined by depth H, width W, and length L and were scaled with the cavity-entrance boundary-layer thickness δ. Heating was measured using global phosphor thermography methods. The reference documents contain an in-depth presentation of the literature survey; and, they describe the multitude of idealized cavity geometries tested to establish the effects of length, width, depth, entry/exit/sidewall angles, orientation, surface curvature, and the fluid dynamic effects of Mach number, Reynolds number, and boundary-layer thickness. Preliminary analysis of these data enabled the development of the assessment methods that form the foundation of the CHT as reported by Anderson et al. [7].

A discussion of the cavity flow physics and a more refined analysis of the laminar-entry heating augmentation or bump factor (BF) was presented in [8] for open-flow (short) cavities where the flow skips over the cavity and for closed-flow (long) cavities where the flow enters the cavity and impinges on the floor. Open cavities have a nominal $L/H < 10$, while closed cavities are nominally $L/H > 14$. The transitional-cavity region between $L/H = 10$ and 14 may be unsteady as the flow oscillates back and forth between the two steady flow regimes. A combined single-curve parametric variation for the floor-averaged BF and centerline endwall maximum BF was derived, as was a model of the heating-wake decay downstream of the cavity. Additionally, uncertainty limits on the correlation curve coefficients and prediction limits about the correlation curves were also provided.

A limited number of closed-flow turbulent test cases were obtained as a part of the Mach 6 cavity experiments to baseline the heating levels for rectangular geometry variations [3]. Using these data, the above-cited laminar correlations have now been extended to include turbulent boundary-layer inflow conditions. The turbulent data were originally reduced and reported using laminar computational solutions for entry reference conditions because turbulent solutions were unavailable. Turbulent solutions have since been developed, and the data have been rereduced with these new entry conditions.

Presented as Paper 2009-1400 at the 47th AIAA Aerospace Sciences Meeting, Orlando, FL, 5–8 January 2009; received 26 August 2009; revision received 31 March 2010; accepted for publication 28 January 2010.

*Senior Research Engineer, Aerothermodynamics Branch. Associate Fellow AIAA.

†Senior Research Engineer, Aerothermodynamics Branch. Senior Member AIAA.

The first task in this paper is to present a sample of the rereduced turbulent data. Next, coefficient values in the laminar parameters will be adjusted to minimize turbulent correlation uncertainties. Finally, using this functional relationship as a guide, correlations will be developed for turbulent open-flow cavities using archival data obtained from the literature. The results presented in this paper correlate all known available experimental turbulent-entry cavity flow heating data.

II. Experimental Methods

This section presents a brief discussion of the experimental methods. The test facility is first discussed, followed by a description of the models and cavity design, and an overview of the phosphor thermography data system used to acquire the global heating measurements. Finally, the data reduction and presentation parameters are described.

A. Facility

The LaRC 20-Inch Mach 6 Tunnel was used to develop the turbulent cavity heating database. This conventional, perfect-gas blowdown facility uses air as a test medium. It is described in detail in Micol [9]. Flow properties were determined using the GASPROPS code developed by Hollis [10].

B. Models

A schematic showing the model coordinate system orientation is presented in Fig. 1. The x axis is measured down the length of the model and the z axis is measured normal to the surface. Initially, the origin is at the model leading edge; it is transferred to the cavity entrance for data analysis. A strut-mounted 10-in.-wide by 28-in.-long steel flat-plate model having a blunted leading edge with a radius of 0.125 in. was used for experiments (see Fig. 2). The blunt nose model provides edge Mach numbers of approximately 2.9 to 3 (see [2]) at zero incidence as required to match Orbiter flight surface conditions. The model includes an upstream insert region where boundary-layer trips can be installed, as shown in the figure. Boundary-layer trip hardware and tripping methods developed by Berry et al. [11,12] were used to ensure turbulent flow over the model. Based on the results presented in [12], the height of the trip, k, is determined from $k/\delta = 0.6$ for the present flow conditions. Offdesign test conditions were examined to ensure fully tripped turbulent conditions. A discussion of the boundary-layer trips and the baseline heating data are presented in [3]. The model also includes a 4-in.-wide by 18-in.-long aft region starting 7.5 in. from the nose for test articles. A representative example of the cavity inserts (see [3]) is shown in Fig. 3. They were fabricated using ceramic casting methods as described in Buck et al. [13,14]. After fabrication, the cavity models were coated with a nominal 27-μm-thick mixture of phosphors suspended in a silica-based colloidal binder [15] and sent to quality assurance for measurement and application of small circular locating markers, known as fiducial marks. Cavity size parameters and location on the insert plate are given in Table 1.

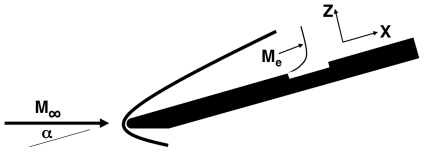

Fig. 1 Model coordinate system.

Fig. 2 Baseline model with 4 by 18 in. ceramic insert.

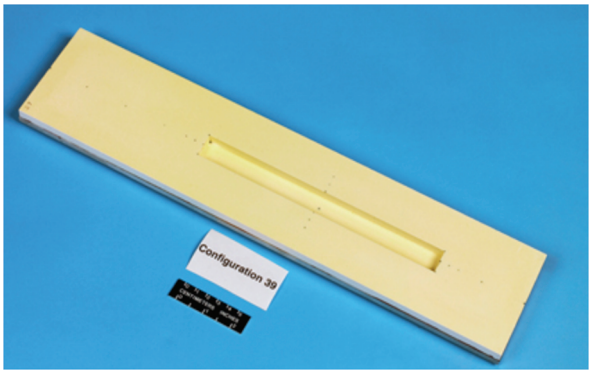

Fig. 3 Sample cavity insert model.

C. Cavity Designs and Test Conditions

Impact-induced cavities must be geometrically and fluid-dynamically scaled for damage-assessment modeling. For the Space Shuttle Orbiter, a maximum cavity-depth constraint can be established based on the thickness of the thermal protection system tiles. Because of the launch configuration, impact damage on the forward portion of the vehicle is likely to be deep and short, in contrast to long, shallow grazing damage that is more likely on the aft portion of the vehicle. Parametric variations used to establish the original cavity heating database were guided by these general considerations.

Typical surface flow conditions for the windward surface of the Space Shuttle Orbiter were obtained from Campbell et al. [16] to establish the parameter variations at the cavity entrance, $(M_e, Re_\theta, \delta)_{\text{Flight}}$. Centerline test-article surface conditions were determined for the tunnel freestream conditions from two-dimensional centerline contour simulations of the baseline geometry using the LAURA code [17,18]. The range of the computationally determined $(M_e, Re_\theta)_{\text{Tunnel}}$ conditions was matched to flight. The boundary-layer thickness ratio $(\delta_{\text{Tunnel}}/\delta_{\text{Flight}})$ was used to scale flight damage scenarios to tunnel scale. Cavity conditions $(M_e, Re_\theta, \delta)_{\text{Tunnel}}$ were taken from the computational solutions at the cavity entrance.

All turbulent-entry data were acquired using closed (long) baseline geometries, each with a flat bottom and rectangular planform and cross section. Tripped turbulent flow was developed over the model surface as discussed in [3]. Specifics of the flight-to-tunnel scaling, cavities, and their designs are included in the database publications by Everhart et al. [3], using methods and hardware developed by Berry et al. [11,12] to ensure fully turbulent flow.

D. Phosphor Thermography Technique

Global surface heating distributions were calculated using the two-color, relative-intensity phosphor thermography method [15]. This is the standard technique for obtaining aeroheating data in the LaRC hypersonic wind tunnels, and it can be used to identify the surface heating effects of complex three-dimensional flow phenomena, which are difficult to examine using conventional discrete-sensor methods. With this method, ceramic wind-tunnel models are coated with phosphor crystals that fluoresce in the red and green regions of the visible light spectrum when illuminated by UV light. The phosphor-coated model is exposed to the heated flow during a

Table 1 Turbulent test matrix

Run	Config	α, deg	Re/L, ft^{-1}	$X_{0,\text{cavity}}$, in.	M_e	Re_θ	Re_θ/M_e	δ, in.	H/δ	W/H	L/H	L/δ	BF_{AVG}	BF_{MAX}
39	27b	0	2.0	10.5	2.93	123	42	0.248	——	——	——	——	——	——
31	27b	0	4.0	18	2.93	150	50	0.312	——	——	——	——	——	——
42	27b	−10	2.0	10.5	2.31	155	67	0.178	——	——	——	——	——	——
226	——	−5	0.6	10.5	2.63	97	37	0.299	——	——	——	——	——	——
215	——	−5	1.9	10.5	2.62	135	51	0.216	——	——	——	——	——	——
117	28	0	2.0	10.5	2.93	123	42	0.248	0.585	2.6	15.6	9.1	1.143	5.454
95	29	0	2.0	10.5	2.93	123	42	0.248	0.612	2.5	18.1	11.1	0.895	5.084
67	30	0	2.0	10.5	2.93	123	42	0.248	0.626	2.5	20.8	13.0	1.007	5.479
87	31	0	2.0	10.5	2.93	123	42	0.248	0.618	2.5	26.5	16.4	0.945	4.668
108	32	0	2.0	10.5	2.93	123	42	0.248	0.578	2.6	34.0	19.7	0.791	4.939
139	36	0	2.0	10.5	2.93	123	42	0.248	1.389	2.4	14.3	19.8	1.264	8.425
140	37	0	2.0	10.5	2.93	123	42	0.248	1.321	2.6	18.2	24.1	1.249	5.741
141	38	0	2.0	10.5	2.93	123	42	0.248	1.386	2.4	20.5	28.4	1.188	8.270
142	39	0	2.0	10.5	2.93	123	42	0.248	1.354	2.5	26.2	35.5	0.999	8.446
143	40	0	2.0	10.5	2.93	123	42	0.248	1.404	2.4	30.5	42.8	0.923	6.378
132	41	0	4.0	18	2.99	150	50	0.312	0.535	2.1	12.8	6.8	1.311	5.585
134	42	0	4.0	18	2.99	150	50	0.312	0.458	2.5	17.9	8.2	1.325	4.754
137	43	0	4.0	18	2.99	150	50	0.312	0.474	2.4	20.6	9.8	1.380	4.550
138	44	0	4.0	18	2.99	150	50	0.312	0.459	2.5	26.5	12.1	1.267	5.990
144	48	0	4.0	18	2.99	150	50	0.312	1.069	2.4	13.8	14.8	1.710	7.509
148	49	0	4.0	18	2.99	150	50	0.312	1.106	2.3	16.3	18.0	1.410	6.019
147	50	0	4.0	18	2.99	150	50	0.312	1.111	2.3	19.1	21.2	1.421	10.956
214	28	−5	1.9	10.5	2.62	135	51	0.216	0.671	2.6	15.6	10.5	1.110	4.595
215	29	−5	1.9	10.5	2.62	135	51	0.216	0.701	2.5	18.1	12.7	1.058	3.727
219	31	−5	1.9	10.5	2.62	135	51	0.216	0.709	2.5	26.5	18.8	1.047	3.370
222	32	−5	1.9	10.5	2.62	135	51	0.216	0.663	2.6	34.0	22.5	1.000	3.726
116	28	−10	2.0	10.5	2.31	155	67	0.178	0.814	2.6	15.6	12.7	1.210	4.130
76	72	−10	2.0	10.5	2.31	155	67	0.178	0.813	7.9	20.0	16.3	0.808	2.449
94	29	−10	2.0	10.5	2.31	155	67	0.178	0.851	2.5	18.1	15.4	1.057	3.778
66	30	−10	2.0	10.5	2.31	155	67	0.178	0.871	2.5	20.8	18.1	1.127	4.780
85	31	−10	2.0	10.5	2.31	155	67	0.178	0.860	2.5	26.5	22.8	1.038	3.608
107	32	−10	2.0	10.5	2.31	155	67	0.178	0.805	2.6	34.0	27.3	1.008	4.248
226	30	−5	0.6	10.5	2.65	99	37	0.299	0.518	2.4	20.8	10.8	0.917	2.727

wind-tunnel run, and the resulting changes in fluorescence intensity of the model are recorded and digitized. The surface temperature distributions are determined from the fluorescence intensities through prior calibrations, reduced to surface heating distributions, and analyzed using the IHEAT [15] code, which implements one-dimensional, semi-infinite-solid heat conduction theory. These distributions may be mapped onto a three-dimensional CAD representation of the test article using the MAP3D [15] code.

E. Data Reduction

Global mappings of the surface heating were converted to a cavity-based reference system by translating the origin from the leading edge of the model to the leading-edge center of each cavity. They were then scaled using the cavity depth and the boundary-layer thickness at the cavity leading edge to yield a scaled-geometry cavity of depth H/δ, width W/H, and length L/H.

Local heating augmentation (or bump factor BF) was used to assess the effect of the cavity on the undisturbed environment. Bump factor is defined as the local heating h_{local} normalized by an averaged reference heating h_{AVG}, yielding $\text{BF} = h_{\text{local}}/h_{\text{AVG}}$. For analysis consistency, h_{AVG} is computed from the measured data, in a scaled-space region ahead of each cavity across the cavity width over the length $-3 \le x/H \le 1$. In this format, $\text{BF} = 1$ becomes the nominal, fully developed, undisturbed condition for a flat plate. This location also avoids a potential bias caused by an expansion-induced heating peak upstream of the cavity leading edge. Two metrics, BF_{AVG} and BF_{MAX}, are used to characterize the cavity heating. Two methods were used to determine BF_{AVG}. In the first method, BF_{AVG} was determined by averaging all imaged data inside the entire cavity. Only a small number of nonfloor pixels were present because the upstream endwall was not visible in the camera imaging and, because of the typically small size of the cavity, only 2–3 pixels were visible in any longitudinal line cut on the downstream cavity endwall. Likewise, only one of the sidewalls was imaged and, typically, only 1–2 pixels were visible in any spanwise line cut. This area averaging greatly reduced noise in the data caused by the low temperatures experienced on the cavity floor for laminar flow conditions. In the second method, BF_{AVG} was determined from the integral of sparse centerline data. Both methods were used in [8] and differences were within data scatter. BF_{MAX} was determined as the maximum centerline value; this value was typically located immediately downstream of the cavity endwall.

III. Computational Simulation of Baseline Model Surface Flow

Boundary-layer edge properties were computed using the LAURA [18,19] code. LAURA is a computational fluid dynamics (CFD) tool specialized for hypersonic reentry physics and chemistry. In the past, the LAURA code has been applied and validated for a range of vehicle shapes and flow conditions including the Space Shuttle Orbiter laminar aerothermodynamic flight data [20], blunt planetary configurations [21,22], and slender lifting bodies [23]. The code is a three-dimensional upwind finite volume solver for the inviscid Euler equations, thin-layer Navier–Stokes, or full Navier–Stokes governing equations. Roe [24] averaging with Harten's [25] entropy fix and Yee's [26] symmetric total-variation-diminishing limiter are used to formulate the inviscid fluxes, and a second-order scheme solves the viscous fluxes. Point relaxation is used to begin the iterative solution while a line relaxation approach is invoked to complete the integration in time to steady state.

The Navier–Stokes equations were solved in simulating the turbulent flow over a flat plate at ground-based test conditions in conjunction with a perfect-gas air thermodynamic model. For this work, it was sufficient to start the turbulent flow at the plate leading edge, and it was modeled using the Cebeci–Smith algebraic turbulence model [27]. A sample of the turbulent heating prediction is compared with experimental measurements in Fig. 4a ($M_e = 2.93$ and $Re_\theta = 150$). Corresponding longitudinal predictions for the M_e,

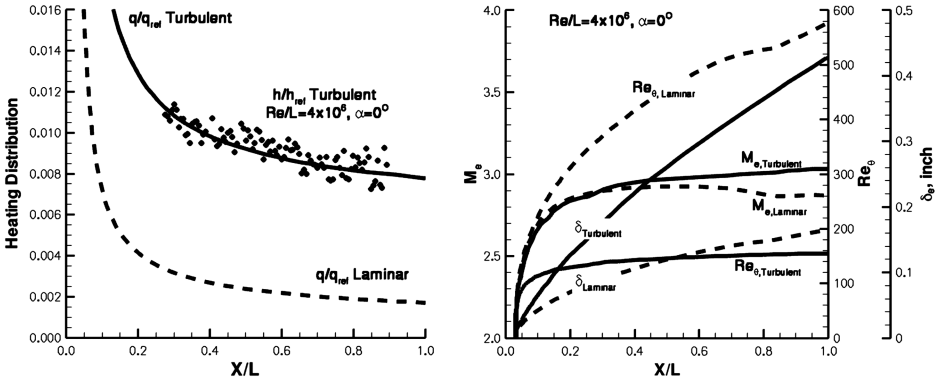

a) Computational and experimental heating b) Surface flow properties

Fig. 4 Representative turbulent CFD simulation.

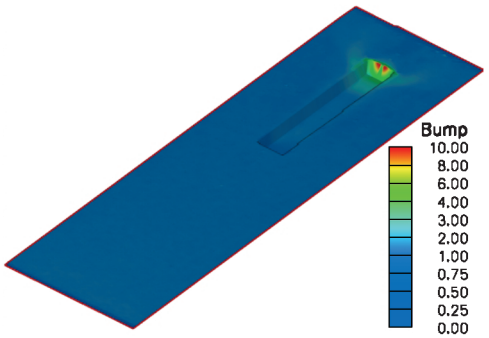

Fig. 5 Effect of length variation for $M_e = 2.99$, $Re_\theta = 150$, $H/\delta = 1.1$, and $L/H \approx 16$.

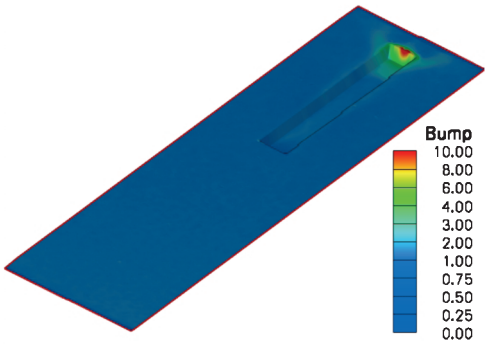

Fig. 6 Effect of length variation for $M_e = 2.99$, $Re_\theta = 150$, and $H/\delta = 1.1$, and $L/H \approx 19$.

Re_θ, and δ, are presented in Fig. 4b. Laminar solutions are also presented in the figures for comparison.

IV. Test Data and Parameter Space

The turbulent test matrix is presented in Table 1, along with the scaled geometry and the BF_{AVG} and BF_{MAX} values for each set of conditions. Typically, a cavity length sweep is presented at nearly constant values of M_e, Re_θ, and H/δ. Turbulent bump-factor image data are presented in Figs. 5 and 6. These demonstrate how the flow physics can change with cavity length. In contrast to the laminar data (see [8]), significant vortex interactions occur on the sides at the top of the turbulent cavity as the flow strongly expands into the cavity, carrying high-temperature fluid. The images show the significant increase in floor heating on the center and in the corner, where vortex scrubbing elevates the temperatures. The complexity of the flowfield is further evidenced by the occurrence of multiple heating peaks on the downstream endwall under some conditions (for example, see Fig. 5). In fact, the peak heating may not occur on the centerline as it does in Fig. 6 because of this flow characteristic.

V. Summary of Laminar Bump-Factor Correlations

Previously developed laminar correlations are presented here in preparation for the turbulent development. Reference [8] graphically demonstrated that neither BF_{AVG} nor BF_{MAX} could be correlated with the individual primary test variables (e.g., M_e, Re_θ, Re_θ/M_e, L/H, H/δ, and L/δ) for laminar flow. Accordingly, the test variables were combined into laminar correlation parameters to describe the variation of heating over a wide range of conditions for both open- and closed-cavity flow physics using aggregate and separate Mach 6 and Mach 10 data. These correlation parameters are given by

$$X = \ell_n\left[M_e^\sigma Re_\theta^\tau\left(\frac{L}{\delta}\right)\right] \qquad Y = \ell_n\left[\left(\frac{H}{\delta}\right)^\alpha\left(1+\frac{L}{H}\right)^\beta \mathrm{BF}\right] \tag{1}$$

For later comparison with the turbulent results, the laminar Mach 6 power coefficients are presented in Table 2.

The Mach 6 correlation parameters for BF_{AVG} and BF_{MAX} were developed using the baseline, rectangular cavity data. These parameters were then input to the commercially available SYSTAT TableCurve 2D program to establish the mathematical relationships for the heating variations. The coefficients a and b in the linear (in transformed log–log space) correlation curve,

$$Y = a + bX \tag{2}$$

were determined by the program, and they are presented in Table 3. Output from the program included upper confidence limits (UCL) and lower confidence limits on the curve coefficients and the linear correlation coefficient R^2 as statistical measures of the goodness of fit to the data. Confidence limits are a measure of the uncertainty in the average value of a coefficient drawn from an existing population. The linear correlation coefficient measures how well the data fit a linear mathematical model, with $R^2 = 1$ providing a perfect fit. Upper prediction limits (UPL) and lower prediction limits measure the ability of the curve to estimate the value of a future observation obtained from the population. By statistical necessity, prediction limits must be wider than confidence limits to capture the additional uncertainty carried by the new data. A discussion of these statistical concepts is provided by Morrison [28].

The Mach 6 laminar correlation curves and the Mach 6 data are presented in Fig. 7 for reference. Open-cavity data are represented by open symbols and the closed-cavity data are represented by closed symbols. All of the data scatter uniformly about the correlation curve

Table 2 Laminar cavity correlation coefficient powers derived from Mach 6 baseline data

Power	BF_{AVG}	BF_{MAX}
α	3.30	3.30
β	2.70	3.70
σ	0.00	0.20
τ	0.10	0.05

Table 3 Laminar cavity correlation coefficient values for $y = a + bx$ fit of Mach 6 baseline data

	BF_{AVG}			BF_{MAX}		
	a	b	DOF-adj R^{2a}	a	b	DOF-adj R^2
Correlation	−2.8251	2.9650	0.9882	−0.6305	3.8695	0.9895
99% UCL	−2.1834	2.9715	——	0.1707	3.8737	——
99% UPL	−2.7237	2.9540	——	−0.5137	3.8588	——

[a]DOF-adj R^2 denotes degree-of-freedom-adjusted R^2.

within the bounds of the 99% prediction limits. Because these data were acquired on a laminar low-temperature flat plate, the scatter band is wider than would be anticipated for a higher temperature turbulent flow. Therefore, it is anticipated that the prediction intervals for the turbulent correlations will be narrower. For clarity, only the laminar curves will be presented for comparison in subsequent figures.

VI. Turbulent Closed-Cavity Heating Correlations

Beginning with the laminar relationships presented in the previous section, the first step in analyzing the turbulent data was to assess whether the application of Eq. (1) and the parameter powers in Table 2 yielded any significant correlation of BF_{AVG} and BF_{MAX}. Direct unadjusted application of these expressions revealed well-defined linear variations associated with each cavity depth. Therefore, the values of the laminar powers provided in Table 2 had to be adjusted to remove the depth effect for the turbulent conditions. New turbulent power coefficients were developed following the process developed in [8]. The laminar powers were iteratively changed to maximize the value of the correlation coefficient R^2. These new turbulent values are presented in Table 4 and the results of the modifications are shown in Fig. 8. Significant improvements in the linearity are provided with the adjusted values that are indicative of the reduced scatter provided by the new correlation. The R^2 for BF_{AVG} has increased from 0.950 to 0.993; the R^2 for BF_{MAX} has increased from 0.930 to 0.988. The degree-of-freedom-adjusted R^2 values are 0.993 for BF_{AVG} and 0.987 for BF_{MAX}, all measures implying a high degree of linear modeling.

Convergence to a local minimum/maximum is a concern in all optimization problems. A correlation development question was whether a single set of correlation parameters could be developed to describe both laminar and turbulent conditions. As a check on the minimization process, the laminar data were tested against the turbulent correlations. The turbulent parameters did describe the gross behavior of the laminar heating, but did so poorly. Therefore, separate closed-cavity correlations of the heating are required for the two boundary-layer states.

As before, correlation curve coefficient values were developed and they are provided in Table 5. Also provided are the 99% upper confidence limits on the curve fit, and the 99% upper prediction limits. Interestingly, the turbulent correlations are nearly parallel to the laminar correlations, as determined by both visual observation in Fig. 8 and by comparison of the slopes (b coefficient) given in Table 3 with those in Table 5. The turbulent 99% uncertainty bounds are narrower than those developed for the laminar correlations because the higher heating reduces the uncertainty in the individual measurements. Fewer data are available over a narrower test space resulting in a broadening of the uncertainty at the extents of the turbulent correlation curve. Therefore, the uncertainty was conservatively estimated using a linear approximation between the end points.

Table 4 Turbulent closed-cavity correlation coefficient powers

Power	BF_{AVG}	BF_{MAX}
α	2.65	3.40
β	3.20	4.20
σ	0.25	0.80
τ	0.35	0.40

Final expressions for the correlations are obtained by substituting Eqs. (1) into Eq. (2), yielding

$$\left(\frac{H}{\delta}\right)^{\alpha}\left(1+\frac{L}{H}\right)^{\beta}\mathrm{BF} = e^{a}\left[M_e^{\sigma}Re_{\theta}^{\tau}\left(\frac{L}{\delta}\right)\right]^{b} \tag{3}$$

where the values of the powers α, β, σ, and τ are obtained from Table 4, and the a and b coefficients are obtained from Table 5.

A relationship for the bump-factor uncertainty, $\Delta BF/BF$, can be obtained by subtracting the linear relationship for the correlation curve from the linear relationship from the upper prediction limit. This is given by

$$\frac{\Delta\mathrm{BF}}{\mathrm{BF}} = e^{(a_{\mathrm{UPL}}-a)}\left[M_e^{\sigma}Re_{\theta}^{\tau}\left(\frac{L}{\delta}\right)\right]^{(b_{\mathrm{UPL}}-b)} - 1 \tag{4}$$

where $\Delta BF = BF_{UPL} - BF$ and, as above, the coefficients are obtained from Table 5. Uncertainties in the turbulent closed-cavity correlations are given as

$$\left(\frac{\Delta\mathrm{BF}}{\mathrm{BF}}\right)_{\mathrm{AVG,Turb}} = 1.3457\left[M_e^{0.25}Re_{\theta}^{0.35}\left(\frac{L}{\delta}\right)\right]^{0.0028} - 1 = 0.35 \tag{5}$$

and

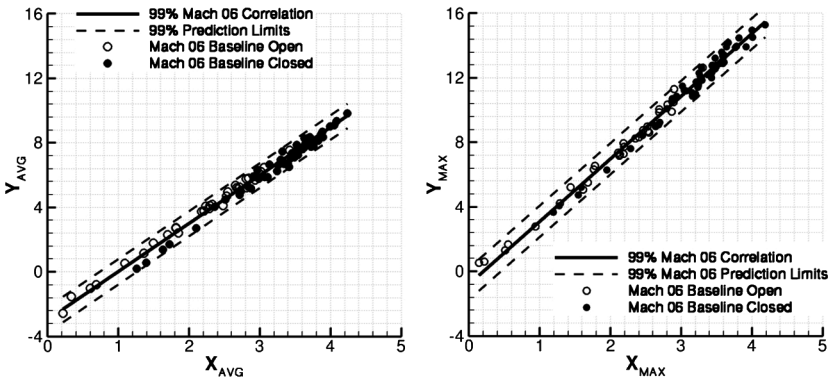

a) Cavity floor correlation **b) Cavity endwall maximum correlation**

Fig. 7 Laminar baseline Mach 6 correlation.

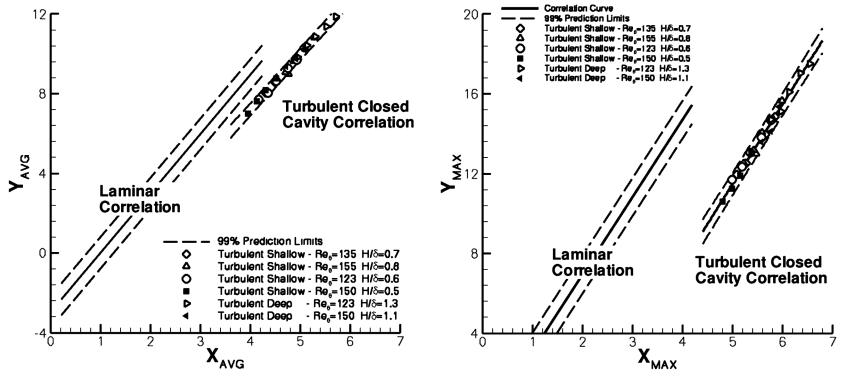

a) Floor average **b) Endwall max**

Fig. 8 Turbulent data correlation using turbulent coefficients, including 99% uncertainty analysis.

$$\left(\frac{\Delta \mathrm{BF}}{\mathrm{BF}}\right)_{\mathrm{MAX,Turb}} = 1.6991\left[M_e^{0.80} Re_\theta^{0.40}\left(\frac{L}{\delta}\right)\right]^{0.0094} - 1 = 0.70 \tag{6}$$

Reflecting the lower temperature measurements, larger uncertainties were present for the laminar correlations developed in [8]. For comparison, they are

$$\left(\frac{\Delta \mathrm{BF}}{\mathrm{BF}}\right)_{\mathrm{AVG,Lam}} = 0.75 \tag{7}$$

and

$$\left(\frac{\Delta \mathrm{BF}}{\mathrm{BF}}\right)_{\mathrm{MAX,Lam}} = 1.28 \tag{8}$$

VII. Turbulent Open-Cavity Heating Correlations

Fully turbulent closed-cavity heating data were not discovered in the open literature; however, several sources of turbulent open-cavity data with sufficient analysis information for obtaining cavity floor averages were available. Because all of the archival data were acquired using discrete sensors, measurements in the vicinity of the endwall top edge were difficult to obtain, allowing only extrapolated peak values containing large uncertainties. Accordingly, only correlations using the floor averages (an integral process with less inherent error) were attempted. The data sources where the boundary layer entering the cavity is turbulent are Charwat et al. [29,30], Emery [31], Netterfield and Hillier [32], and Thomann [33]. These data were acquired on the wind-tunnel floor and on an axisymmetric cone. Data acquired by Hahn [34] (axisymmetric cylinder) and Nestler et al. [35] (flat plate) had transitional boundary layers entering the cavity. (As a side note, the original definitions of open and closed cavities originate with Charwat et al. [29,30].) According to Nestler et al. [35], the heating augmentation for transitional flow will be the same as that for turbulent flow over a separated cavity. This important hypothesis for cavity design and impact-damage assessment will be demonstrated as erroneous.

These archival data represent an extremely wide range of turbulent flow and geometric conditions that are tabulated in Table 6 and plotted as $\mathrm{BF_{AVG}}$ versus L/δ in Fig. 9. Cavity-entry Mach number varies from 1.8 to 9, momentum-thickness Reynolds number varies from 2098 to 32,288, depth H/δ varies from 0.44 to 4.17, and length L/δ varies from 0.33 to 44. All of the cavities have a rectangular (or nearly rectangular) profile geometry with a width W/H that varies from 1.25 for the three-dimensional cases to infinity for the axisymmetric cases. In many cases, the required boundary-layer parameters were unavailable in the reports. Referencing White [36], estimates of the turbulent thicknesses were obtained from

$$\frac{\delta}{x} = 0.37 Re_s^{-\frac{1}{5}} \quad \text{and} \quad \frac{\theta}{x} = 0.036 Re_s^{-\frac{1}{5}} \tag{9}$$

where Re_S is the Reynolds number based on boundary-layer run length. Combining Eqs. (9) yields

$$\frac{\theta}{\delta} = 0.097 \tag{10}$$

Equation (10) was used to determine the momentum-thickness Reynolds number where required. Average floor-heating data were obtained by integrating cavity-heating distributions when not provided directly in report figures.

An initial attempt at correlating the turbulent open cavity $\mathrm{BF_{AVG}}$ was made using Eqs. (1) and the turbulent closed-cavity powers from Table 4. While the turbulent closed-cavity correlation collapsed each individual data set, the different data sets were widely and unacceptably separated. Unlike the single-curve correlation provided for laminar open and closed cavities in [8], two distinct correlations are required for turbulent open and closed cavities. A successful direct application of the laminar correlation powers (Table 2) to the turbulent open-cavity data is presented in Fig. 10. No attempt at further scatter-reduction via modification of the laminar powers was attempted. The implication of this collapse is that cavity heating is a vortex- and gradient-driven problem in which the flow gradients for laminar open and closed cavities are relatively benign, as they are for open turbulent cavities. Thus, the flows scale similarly, providing a single set of correlation powers. A definitive statement regarding the behavior of $\mathrm{BF_{MAX}}$ cannot be made without appropriate data; however, similar behavior is anticipated. Closed turbulent cavities provide three distinct internal flowfields that develop severe turning gradients. These differences result in much higher heating levels and greater variability along the cavity floor, and they are reflected in the powers in the scaling parameters and in the turbulent curve-fit slopes. With the correct turbulent scaling defined, it is now observationally clear in Fig. 10 that transitional-entry cavities are outliers, and these data should be excluded.

Table 5 Turbulent closed-cavity correlation coefficient values for $y = a + bx$ fit of Mach 6 baseline data

	$\mathrm{BF_{AVG}}$			$\mathrm{BF_{MAX}}$		
	a	b	DOF-adj R^2	a	b	DOF-adj R^2
Correlation	−3.8686	2.7683	0.9925	−8.4946	3.9942	0.9879
99% UCL	−3.4116	2.8636	——	−7.1230	4.2394	——
99% UPL	−3.5717	2.7711	——	−7.9645	4.0036	——

Table 6 Archival cavity-floor heating data, geometry, and conditions

Configuration	M_e	Re_θ	δ, in.	H, in.	W, in.	L, in.	H/δ	W/H	L/H	L/δ	BF_{AVG}
					Charwat et al. [29,30]						
Tunnel floor	2.1	7,943	0.425	0.250	3.00	0.750	0.59	12.00	3.0	1.76	1.100
Tunnel floor	2.9	6,310	0.540	0.250	3.00	0.750	0.46	12.00	3.0	1.39	0.900
Tunnel floor	3.5	4,409	0.568	0.250	3.00	0.750	0.44	12.00	3.0	1.32	0.850
Tunnel floor	2.1	7,943	0.425	0.250	3.00	1.500	0.59	12.00	6.0	3.53	1.090
Tunnel floor	2.9	6,310	0.540	0.250	3.00	1.500	0.46	12.00	6.0	2.78	0.920
Tunnel floor	3.5	4,409	0.568	0.250	3.00	1.500	0.44	12.00	6.0	2.64	0.860
Tunnel floor	2.1	7,943	0.425	0.250	3.00	2.250	0.59	12.00	9.0	5.29	1.150
Tunnel floor	2.9	6,310	0.540	0.250	3.00	2.250	0.46	12.00	9.0	4.17	0.980
Tunnel floor	3.5	4,409	0.568	0.250	3.00	2.250	0.44	12.00	9.0	3.96	0.880
Tunnel floor	2.1	7,943	0.425	0.500	3.00	1.500	1.18	6.00	3.0	3.53	0.680
Tunnel floor	2.9	6,310	0.540	0.500	3.00	1.500	0.93	6.00	3.0	2.78	0.650
Tunnel floor	3.5	4,409	0.568	0.500	3.00	1.500	0.88	6.00	3.0	2.64	0.640
Tunnel floor	2.1	7,943	0.425	0.500	3.00	3.000	1.18	6.00	6.0	7.06	0.660
Tunnel floor	2.9	6,310	0.540	0.500	3.00	3.000	0.93	6.00	6.0	5.56	0.530
Tunnel floor	3.5	4,409	0.568	0.500	3.00	3.000	0.88	6.00	6.0	5.29	0.500
Tunnel floor	2.1	7,943	0.425	0.500	3.00	4.500	1.18	6.00	9.0	10.59	0.580
Tunnel floor	2.9	6,310	0.540	0.500	3.00	4.500	0.93	6.00	9.0	8.33	0.520
Tunnel floor	3.5	4,409	0.568	0.500	3.00	4.500	0.88	6.00	9.0	7.93	0.420
Tunnel floor	2.1	7,943	0.425	0.250	3.00	3.000	0.59	12.00	12.0	7.06	1.250
Tunnel floor	2.9	6,310	0.540	0.250	3.00	3.000	0.46	12.00	12.0	5.56	1.120
Tunnel floor	3.5	4,409	0.568	0.250	3.00	3.000	0.44	12.00	12.0	5.29	0.940
					Emery [31]						
Tunnel floor	2.9	32,288	0.150	0.250	0.75	0.75	1.67	3.00	3.0	5.00	0.602
Tunnel floor	2.9	32,288	0.150	0.250	0.75	1.00	1.67	3.00	4.0	6.67	0.563
Tunnel floor	2.9	32,288	0.150	0.250	0.75	1.25	1.67	3.00	5.0	8.33	0.462
Tunnel floor	2.9	32,288	0.150	0.250	0.75	1.50	1.67	3.00	6.0	10.00	0.434
Tunnel floor	2.9	32,288	0.150	0.250	0.75	1.75	1.67	3.00	7.0	11.67	0.403
Tunnel floor	2.9	32,288	0.150	0.250	0.75	2.00	1.67	3.00	8.0	13.33	0.385
Tunnel floor	2.9	32,288	0.150	0.250	0.75	2.25	1.67	3.00	9.0	15.00	0.407
Tunnel floor	2.9	32,288	0.150	0.250	0.75	2.50	1.67	3.00	10.0	16.67	0.475
Tunnel floor	2.9	32,288	0.150	0.250	0.75	2.75	1.67	3.00	11.0	18.33	0.478
					Hahn [34]						
Axisym cyl	6.3	4,188	4.584	19.100	——	101.80	4.17	——	5.3	22.21	1.255
Axisym cyl	6.3	2,797	4.584	19.100	——	152.40	4.17	——	8.0	33.25	1.470
Axisym cyl	6.3	2,098	4.584	19.100	——	203.20	4.17	——	10.6	44.33	1.800
					Netterfield and Hillier [32]						
Axisym cone	9.0	9,925	0.236	0.098	——	0.079	0.42	——	0.8	0.33	0.850
Axisym cone	9.0	9,925	0.236	0.098	——	0.157	0.42	——	1.6	0.67	0.658
Axisym cone	9.0	9,925	0.236	0.098	——	0.236	0.42	——	2.4	1.00	0.520
Axisym cone	9.0	32,109	0.236	0.098	——	0.079	0.42	——	0.8	0.33	0.410
Axisym cone	9.0	32,109	0.236	0.098	——	0.157	0.42	——	1.6	0.67	0.430
Axisym cone	9.0	32,109	0.236	0.098	——	0.236	0.42	——	2.4	1.00	0.500
					Thomann [33]						
Tunnel floor	1.8	12,300	0.424	0.787	3.00	2.362	1.86	3.80	3.0	5.57	0.590
Tunnel floor	1.8	12,300	0.424	0.394	3.00	2.362	0.93	7.60	6.0	5.57	0.554
Tunnel floor	1.8	12,300	0.424	0.197	3.00	2.362	0.46	15.20	12.0	5.57	0.709
					Nestler et al. [35]						
Flat plate	8.5	9,571	0.320	1.000	4.00	5.0	4.17	3.13	5.0	15.6	0.515
Flat plate	8.5	9,571	0.320	0.800	4.00	12.0	4.17	2.50	15.0	37.5	1.211
Flat plate	8.5	9,571	0.320	0.400	4.00	12.0	4.17	1.25	30.0	37.5	0.702

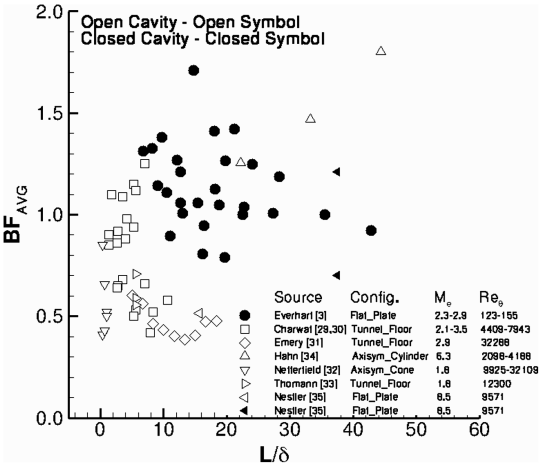

Fig. 9 Archival turbulent-entry open-cavity-floor-averaged heating augmentation data.

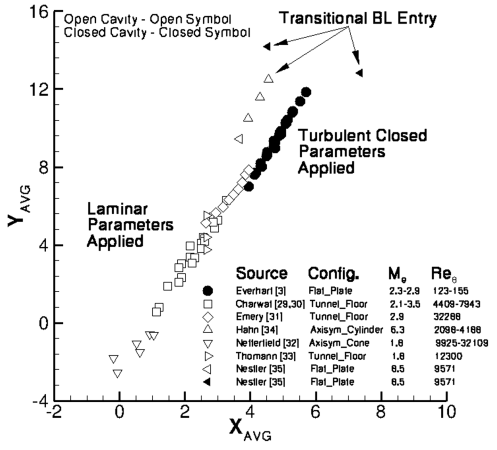

Fig. 10 Correlated turbulent cavity-floor-averaged heating augmentation.

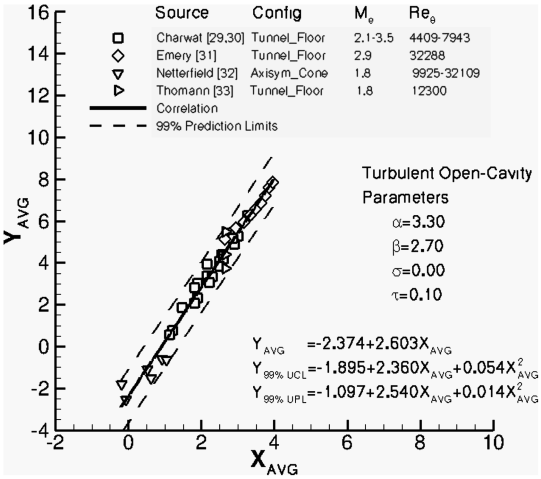

Fig. 11 Turbulent open-cavity-floor-averaged heating augmentation.

Figure 11 presents the turbulent open-cavity correlation curves. The powers and curve coefficients are presented in Tables 7 and 8, respectively. As with the turbulent closed cavity, curve-fit coefficients, confidence limits, and prediction limits were determined at the 99% level of uncertainty using the SYSTAT TableCurve 2D program. Analytical expressions for the open-cavity uncertainties can be obtained following the procedure presented in Eqs. (3–6).

VIII. Correlation Applicability

When developing the laminar correlations (see Fig. 7 and [8]), the heating data obtained on the flat-plate models were carefully screened to ensure the existence of laminar-exit flow conditions. This was accomplished by comparing heating levels obtained on baseline and cavity-installed models with tripped, fully turbulent flow. The ranges of the laminar flow conditions are summarized in Table 9. Correlations developed with these data exhibit an exceptional degree of linearity, deviating only when nonlaminar exit conditions are encountered. As shown in Table 9, the fully turbulent closed-cavity correlations developed herein used a smaller subset of the laminar test conditions. However, as shown in Fig. 8, these correlations retain the linear characteristic, though offset from the laminar curves. A third strong demonstration of the linear trend is provided by the fully turbulent, open-cavity correlation presented in Fig. 11. The parameter range for these data (see Table 9) is very wide, covering M_e from 1.8 to 9.0 and Re_θ from 4409 to 32,288. Therefore, it is concluded that the proper descriptive correlation parameters for cavity flow heating and their functional relationships have been established, as long as the spanwise symmetry of the flowfield is maintained, as it is with all data used for these developments, and in the development of the CHT [7]. If spanwise geometric symmetry is not present, such as a damage situation with a rotated or skewed cavity, then engineering judgment and a knowledge of the flow environment must be used when defining the cavity geometry used for estimating the heating augmentation (see [7]).

Table 7 Turbulent open-cavity correlation coefficient powers

Power	BF_{AVG}
α	3.30
β	2.70
σ	0.00
τ	0.10

Table 8 Turbulent open-cavity correlation coefficient values for $y = a + bx$ fit of archival data

	BF_{AVG}			
	a	b	c	DOF-adj R^2
Correlation	−2.3741	2.6034	0.0000	0.9752
99% UCL	−1.8950	2.3604	0.0538	——
99% UPL	−1.0967	2.5399	0.0139	——

Table 9 Range of parameters used in correlation development

Parameter	Laminar in, laminar out open and closed	Fully turbulent closed	Fully turbulent open
M_e	1.3–3.2	2.3–3.0	1.8–9.0
Re_θ	43–725	97–155	4409–32,288
H/δ	0.1–2.4	0.46–1.34	0.42–1.86
L/H	7–30	13–34	3–12
L/δ	0.7–34	7–43	0.33–18

As a turbulent application example, consider a 1-in.-deep damage site in a shuttle tile. If the damage is no longer than 10 in., it can be analyzed as an open cavity ($L/H \leq 10$). Accordingly, orientation is not important because the flow does not directly enter the cavity and impinge on the floor. Furthermore, if the boundary layer is 2 in. thick or greater, it can be considered a shallow cavity ($H/\delta < 0.5$) and the heating will be further reduced because the flow turning gradients are small, and because the relatively thick boundary layer insulates the cavity. Flight experience has shown that 98% of the damage sites on the shuttle are less than 10 in. in length.

IX. Conclusions

A massive cavity-heating database was generated and documented to support development of the current laminar analysis methods provided in the CHT (version 3). This tool is used for impact-damage assessment of the shuttle thermal protection system. The laminar cavity data were recently reanalyzed and new correlations with quantifiable uncertainty levels were developed and reported for the floor-averaged bump factor (or heating augmentation) and the maximum endwall bump factor.

Included in the original database were limited turbulent closed-cavity test cases. These data were used for comparison with laminar heating levels to assess the boundary-layer state within and downstream of the cavity. New turbulent computational solutions of the flowfield on the no-cavity base model have provided the proper cavity entrance conditions that allow full reduction of the data, enabling evaluation of the existing turbulent cavity analysis methods using globally acquired heating data.

The new turbulent solutions also have enabled development of new turbulent closed-cavity correlations. A direct application of the laminar cavity heating correlations to the turbulent closed-cavity data captured the variations of the cavity-floor averaged heating and the maximum heating on the cavity endwall; however, data scatter was larger than desired. As a result, new turbulent coefficients were derived, and they are very descriptive of cavity heating under common surface flow and geometric variations, having linear correlation coefficients R^2 that exceed 0.98.

New turbulent open-cavity-floor heating correlations have been developed using archival data retrieved from the literature. These data cover an extremely wide range of flow conditions, including M_e from 1.8 to 9.0 and Re_θ from 4409 to 32,288. The geometries include rectangular cavities in flat plates and wind-tunnel walls and axisymmetric cavities on bodies of revolution. Linear correlation coefficients R^2 exceed 0.97. Historical flight experience indicates that these correlations should encompass 98% of the impact-damage geometries experienced on the shuttle.

In all cases, for laminar and turbulent boundary layers and for open-flow and closed-flow cavity conditions, the correlation parameters proved descriptive of the heating, providing strongly linear variations with well-defined uncertainty specifications. Current and future vehicle programs should benefit from their application to impact-damage assessment and to vehicle risk reduction efforts during design.

References

[1] "Report of the Columbia Accident Investigation Board," Vol. 1, NASA, Aug. 2003.

[2] Everhart, J. L., Berger, K, T., Bey, K. S., Merski, N. R., and Wood, W. A., "Cavity Heating Experiments Supporting Shuttle Columbia Accident Investigation," NASA TM 2006-214528, 2006.

[3] Everhart, J. L., Berger, K. T., Brauckmann, G. J., Merski, N. R. , and Wood, W. A., "Parametric Cavity Heating Experiments Supporting Shuttle Orbiter Return to Flight," NASA Johnson Space Center, Rept. EG-SS-06-04, Houston, TX, 2007.

[4] Everhart, J. L., Alter, S. J., Merski, N. R., Wood, W. A., and Prabhu, R. K., "Pressure Gradient Effects on Hypersonic Cavity Flow Heating," 44th AIAA Aerospace Sciences Meeting and Exhibit, AIAA Paper 2006-0185, Reno, NV, Jan. 9–12, 2006.

[5] Everhart, J. L., Berger, K. T., Merski, N. R., Wood, W. A., Hollingsworth, K. E., Hyatt, A. J., and Prabhu, R. K., "Aero-Heating of Shallow Cavities in Hypersonic Freestream Flow," NASA Johnson Space Center, Rept. EG-SS-06-07, Houston, TX, 2007.

[6] Everhart, J. L., Hollingsworth, K. E., Erickson, D. W., Merski, N. R., and Prabhu, R. K., "Real-Cavity Heating Experiments Supporting Shuttle Orbiter Return to Flight," NASA Johnson Space Center, Rept. EG-SS-07-01, Houston, TX, Feb. 2007.

[7] Anderson, B., Hyatt, J., Wang, K. C., Everhart, J., Greene, F., Pulsonetti, M., et al., "The Cavity Heating Tool," TM ATA-AH-TM-2005-079, The Boeing Co., NASA Space Systems, Houston, TX, Dec. 2005.

[8] Everhart, J. L., "Supersonic/Hypersonic Laminar Heating Correlations for Rectangular and Impact-Induced Open and Closed Cavities," *Journal of Spacecraft and Rockets*, Vol. 46, No. 3, 2009, pp. 545–560. doi:10.2514/1.36830; also 46th AIAA Aerospace Sciences Meeting and Exhibit, AIAA Paper 2008-1283, Reno, NV, Jan. 2008.

[9] Micol, J. R., "Hypersonic Aerodynamic/Aerothermodynamic Testing Capabilities at Langley Research Center: Aerothermodynamic Facilities Complex," AIAA Paper 95-2107, June 1995.

[10] Hollis, B. R., "Real-Gas Flow Properties for NASA Langley Research Center Aerothermodynamic Facilities Complex Wind Tunnels," NASA CR 4755, Sept. 1996.

[11] Berry, S. A., Difulvio, M., and Kowalkowski, M. K., "Forced Boundary-Layer Transition on X-43 (Hyper-X) in NASA LaRC 20-Inch Mach 6 Air Tunnel," NASA TM-2000-210316, Aug. 2000.

[12] Berry, S. A., Auslender, A. H., Dilley, A. D., and Calleja, J. J., "Hypersonic Boundary-Layer Trip Development for Hyper-X," *Journal of Spacecraft and Rockets*, Vol. 38, No. 6, 2001, pp. 853–864. doi:10.2514/2.3775

[13] Buck, G. M., and Vasques, P., "An Investment Ceramic Slip-Casting Technique for Net-Form, Precision, Detailed Casting of Ceramic Models," U.S. Patent 5,266,252, Nov. 1993.

[14] Buck, G. M., Powers, M. A., Nevins, S. C., Griffith, M. S., Verneris, P. H., and Wainwright, G. A., "Rapid Fabrication of Flat Plate Cavity Phosphor Thermography Test Models for Shuttle Return-to-Flight Aero-Heating," NASA TM 2006-214508, 2006.

[15] Merski, N. R., "An Improved Two-Color Relative-Intensity Phosphor Thermography Method for Hypersonic Wind Tunnel Aeroheating Measurements," NASA CDTP-1017, Feb. 2001.

[16] Campbell, C. H., Wang, K. C., An, M. Y., Tam, L. T., and Bouslog, S. A., "Orbiter Boundary-Layer Working Group, Numerical Flow Field Analysis Data," NASA Johnson Space Center, Rept. 26816, Houston, TX, Dec. 1994.

[17] Gnoffo, P. A., Gupta, R. N., and Shinn, J. L., "Conservation Equations and Physical Models for Hypersonic Air Flows in Thermal and Chemical Nonequilibrium," NASA TP 2867, Feb. 1989.

[18] Gnoffo, P. A., "An Upwind-Biased, Point-Implicit Relaxation Algorithm for Viscous, Compressible Perfect Gas Flows," NASA TP 2953, Feb. 1990.

[19] Gnoffo, P. A., Gupta, R. N., and Shinn, J., "Conservation Equations and Physical Models for Hypersonic Air Flows in Thermal and Chemical Nonequilibrium," NASA TP 2867, 1989.

[20] Gnoffo, P. A., and Weilmuenster, K. J., "Multiblock Analysis for Shuttle Orbiter Re-Entry Heating from Mach 24 to Mach 12," AIAA Paper 93-2813, July 1993.

[21] Gnoffo, P. A., Weilmuenster, K. J., Braun, R. D., and Cruz, C. I., "Influence of Sonic-Line Location on Mars Pathfinder Probe Aerothermodynamics," *Journal of Spacecraft and Rockets*, Vol. 33, No. 2, 1996, pp. 169–177. doi:10.2514/3.26737

[22] Gnoffo, P. A., Braun, R. D., Weilmuenster, K. J., Mitcheltree, R. A., Engelund, W. C., and Powell, R. W., "Prediction and Validation of Mars Pathfinder Hypersonic Aerodynamic Database," *Journal of Spacecraft and Rockets*, Vol. 36, No. 3, 1999, pp. 367–373. doi:10.2514/2.3455

[23] Thompson, R. A., and Gnoffo, P. A., "Application of the LAURA Code for Slender-Vehicle Aerothermodynamics," *Journal of Spacecraft and Rockets*, Vol. 29, No. 1, 1992, pp. 16–23. doi:10.2514/3.26309

[24] Roe, P. L., "Approximate Riemann Solvers, Parameter Vectors and Difference Schemes," *Journal of Computational Physics*, Vol. 43, No. 2, 1981, pp. 357–372. doi:10.1016/0021-9991(81)90128-5

[25] Harten, A., "High Resolution Schemes for Hyperbolic Conservation Laws," *Journal of Computational Physics*, Vol. 49, No. 3, 1983, pp. 357–393. doi:10.1016/0021-9991(83)90136-5

[26] Yee, H. C., "On Symmetric and Upwind TVD Schemes," NASA TM 88325, 1990.

[27] Cebeci, T., "Behavior of Turbulent Flow near a Porous Wall with Pressure Gradient," *AIAA Journal*, Vol. 8, No. 12, Dec. 1970, pp. 2152–2156. doi:10.2514/3.6079

[28] Morrison, D. F., *Applied Linear Statistical Methods*, Prentice–Hall, Englewood Cliffs, NJ, 1983.

[29] Charwat, A. F., Roos, J. N., Dewey, C. F., Jr., and Hitz, J. A., "An Investigation of Separated Flows—Part I, The Pressure Field," *Journal of the Aerospace Sciences*, Vol. 28, No. 6, June 1961, pp. 457–470.

[30] Charwat, A. F., Dewey, C. F., Roos, J. N., and Hitz, J. A., "An Investigation of Separated Flows—Part II, Flow in the Cavity and Heat Transfer," *Journal of the Aerospace Sciences*, Vol. 28, No. 7, July 1961, pp. 513–527.

[31] Emery, A. F., "Recompression Step Heat Transfer Coefficients for Supersonic Open Cavity Flow," *Journal of Heat Transfer*, Vol. 91, Feb. 1969, pp. 168–170.

[32] Netterfield, M., and Hillier, R., "Experiment and Computation in Hypersonic Cavity Flows," 20th Fluid Dynamics, Plasma Dynamics and Lasers Conference, AIAA Paper 89-1842, Buffalo, NY, June 1989.

[33] Thomann, H., "Measurement of Heat Transfer and Recovery Temperature in Regions of Separated Flow at a Mach Number of 1.8," Aeronautical Research Inst. of Sweden (FFA), Rept. 82, Bromma, Sweden, 1959.

[34] Hahn, M., "Experimental Investigation of Separated Flows over a Cavity at Hypersonic Speed," *AIAA Journal*, Vol. 7, No. 6, June 1969, pp. 1092–1098. doi:10.2514/3.5280; also AIAA Paper 68-672, 1968.

[35] Nestler, D. E., Saydah, A. R., and Auxer, W. L., "Heat Transfer to Steps and Cavities in Hypersonic Turbulent Flow," Fluid and Plasma Dynamics Conference, Los Angeles, AIAA Paper 68-673, 1968.

[36] White, F. M., *Viscous Fluid Flow*, 1st ed., McGraw–Hill, New York, 1974.

G. Palmer
Associate Editor